



Preparing copper doped carbon nitride from melamine templated crystalline copper chloride for Fenton-like catalysis

Jian-Nan Zhu^a, Xiao-Qin Zhu^a, Fang-Fang Cheng^b, Peng Li^a, Fei Wang^a, Ya-Wen Xiao^a, Wei-Wei Xiong^{a,*}

^a Key Laboratory of Flexible Electronics (KLOFE), Institute of Advanced Materials (IAM), Jiangsu National Synergetic Innovation Center for Advanced Materials (SICAM), Nanjing Tech University (NanjingTech), 30 South Puzhu Road, Nanjing, 211816, PR China

^b School of Pharmacy, Nanjing University of Chinese Medicine, Nanjing, 210023, PR China



ARTICLE INFO

Keywords:

Copper chloride
Melamine
Cu-g-C₃N₄
Cu-N_x species
Fenton-like catalysis

ABSTRACT

Heterogeneous catalysts prepared by doping metal ions in g-C₃N₄ have been demonstrated as a type of promising alternative to the traditional homogeneous Fenton catalysts. The metal-N_x active sites of metal doped g-C₃N₄ composites are responsible for their enhanced catalytic activity. However, it is very difficult to achieve high content of metal-N_x species through pyrolyzing the physical mixtures of metal salts and g-C₃N₄ or melamine. In this work, copper doped g-C₃N₄ composites were synthesized by pyrolyzing a melamine templated crystalline copper chloride [H₂mela]₂[CuCl₅]Cl. High content of Cu-N_x species were formed in these Cu-g-C₃N₄ composites. Compared with the catalysts prepared by pyrolyzing the physical mixtures of CuCl₂ and g-C₃N₄/mela, the Cu-g-C₃N₄ composites exhibited enhanced catalytic activities for the degradation of RhB, MO, and MB. This work suggests that crystalline metal chlorides contained melamine ligands could be employed as efficient precursors for synthesizing metal doped g-C₃N₄ composites with high content of metal-N_x species.

1. Introduction

Wastewater pollution from industrial organic dyes has attracted increasing attentions due to their toxicity and difficulty in degradation, which pose a serious threat to human health and natural environment [1–3]. Fortunately, many effective treatments have been developed to remove organic dyes from wastewater, such as physical adsorption [4], biodegradation [5,6], and membrane separation [7]. Among these treatments, advanced oxidation processes (AOPs) have been acknowledged as a type of powerful technology to deal with wastewater pollution by decomposing organic dyes via hydroxyl radicals (OH) [8–11]. As one of the advanced oxidation processes, Fenton process has been widely applied in industrial wastewater treatment [12–16]. This homogeneous reaction technology generates hydroxyl radicals from H₂O₂ decomposition in Fe²⁺/Fe³⁺ redox pair system. However, there are some disadvantages in traditional Fenton process, such as limited pH range (pH = 2–3), large consumption of Fe²⁺, massive formation of iron mud after neutralization [17]. Furthermore, the slow conversion from Fe³⁺ to Fe²⁺ can also restrict the production of reactive hydroxyl radicals and limit the degradation performance [18]. In order to solve these problems, heterogeneous Fenton-like catalysts have been exploited and proved as a type of promising alternative to the

traditional homogeneous Fenton catalysts.

Choosing chemical stable matrix to encapsulate metal ions is important for the preparation of efficient heterogeneous Fenton-like catalysts. Graphitic carbon nitride (g-C₃N₄) featured graphite-like two-dimensional sheet could be used as an ideal matrix owing to their excellent chemical stability, nontoxicity, and tunable photoelectronic properties [19–23]. In addition, the abundant “nitrogen pots” made up by six nitrogen atoms in g-C₃N₄ sheet provide numerous active trapping sites to encapsulate metal ions. Besides these unique qualities, g-C₃N₄ can be easily prepared through thermal polymerization of some cheap N-rich raw chemicals [24], such as melamine [25], dicyandiamide [26], cyanamide [27], urea [28], and thiourea [29]. Actually, various metal-g-C₃N₄ composites have been prepared by heat treatment of the mixture of metal salts and g-C₃N₄ or other N-rich raw chemicals. These metal-g-C₃N₄ composites displayed promising photocatalytic properties. However, investigation of these materials in the Fenton reactions is still in infancy stage, thus more efforts are required to dedicate in this research area. In order to enhance the Fenton reaction efficiency, harvesting more metal ions in the “nitrogen pots” of g-C₃N₄ sheets would offer more catalytic active sites for redox process. Therefore, pyrolyzing proper precursors to obtain highly dispersed metal-g-C₃N₄ composites is desirable. Typical fabrications were carried out by heating the physical

* Corresponding author.

E-mail address: iamwwxiong@njtech.edu.cn (W.-W. Xiong).

mixtures of metal salts and g-C₃N₄ or melamine, where the metal species and g-C₃N₄ were integrated at micro or nano-scale, leading to low dispersion of the resulted metal-g-C₃N₄ composites. Crystalline metal chlorides templated by protonated melamine can be chosen as a good type of precursors for synthesizing highly dispersed metal-g-C₃N₄ composites. Their highly ordered crystal structures ensure the regular arrangement of metal species and melamine at the molecular scale, which is benefit for the interactions between metal ions and nitrogen atoms of melamine under the pyrolysis conditions. Furthermore, the pyrolysis process of metal chlorides could easily release most of chlorine ions in the form of hydrochloric gas, and consequently create favorable conditions for the formation of metal-N bonds. However, to the best of our knowledge, application of melamine templated crystalline metal chlorides as precursors to prepare metal-g-C₃N₄ composites for Fenton reactions has remained unexplored.

Compared with typical Fenton system of Fe species, element copper holds a similar redox capacity, and the Cu⁺/Cu²⁺ pair showed faster redox cycle than Fe²⁺/Fe³⁺ pair, which means Cu²⁺ ion can be easily reduced to Cu⁺ ion by H₂O₂ under the Fenton-like reaction conditions [30]. Based on the above considerations, we selected a melamine templated crystalline copper chloride [H₂mela]₂[CuCl₅]Cl (mela = melamine) as precursor to prepare Cu-g-C₃N₄ composites. This copper chloride possesses alternatively packed negative layers of [CuCl₅]_n³ⁿ⁻ chains and Cl⁻ anions and positive layers of doubly protonated melamine cations. Through a one-step pyrolysis of the copper chloride precursor [H₂mela]₂[CuCl₅]Cl, we synthesized three copper doped g-C₃N₄ composites (CuCN-500/550/580) at different pyrolysis temperatures. Most of chlorine atoms were released in the pyrolysis process, leading to the formation of extensive Cu-N bonds between Cu atoms and g-C₃N₄ nanoflakes. As a consequence, high density Cu content (loading up to 25.9 wt %) was well dispersed in the g-C₃N₄ matrix, which was characterized by PXRD, FTIR, XPS, ICP, SEM, EDS mapping and TEM. Moreover, these Cu-g-C₃N₄ composites could produce hydroxyl radicals via H₂O₂ at neutral pH under light-free condition, indicating that they can be applied as Fenton-like catalysts for the degradation of typical organic dye pollutants. Indeed, all these Cu-g-C₃N₄ composites displayed excellent catalytic activities for the degradation of RhB, MO, and MB. Our studies offered a facile approach for preparing heterogeneous Fenton-like catalysts through the pyrolysis of melamine templated crystalline metal chlorides.

2. Experimental

2.1. Materials

All the chemicals were commercially available and do not require further purification. Copric chloride dihydrate (CuCl₂·2H₂O) was supplied by Shanghai Xinbao fine chemical plant. Melamine (C₃N₆H₆) and anhydrous ethanol were purchased from NanJing WanQing Chemical Glassware Instrument. Hydrochloric acid (HCl, 35–37%) and hydrogen

peroxide (H₂O₂, 30%, w/w) were supplied by Shanghai Ling Feng Chemical Reagent. Rhodamine B (RhB) came from Macklin reagent, China. Methyl orange (MO) was provided by Aladdin Industrial Corporation, China. Methylene blue (MB) was purchased from Tianjin Institute of chemical reagents. Ammonium chloride (NH₄Cl) was purchased from Xilong Chemical.

2.2. Preparation of [H₂mela]₂[CuCl₅]Cl precursor

[H₂mela]₂[CuCl₅]Cl was synthesized by a modified approach of the literature [31] to improve its yield. 6.8 g of CuCl₂·2H₂O (0.04 mol) was dissolved in 300 mL of hydrochloric acid (37%) to form a green solution at room temperature. Then 10 g of melamine (0.08 mol) was added slowly in the above solution with continuous stirring. With the dissolution of melamine in the green solution, a mass of yellow powder was generated quickly. 15.2 g of yellow precipitates were filtered out and washed several times by hydrochloric acid (37%). The obtained products were dried in air overnight. The PXRD pattern of the yellow powder matched well with the simulated PXRD pattern from single-crystal XRD data (Fig. S1), suggesting the phase purity of the products.

2.3. Preparation of g-C₃N₄ and Cu-g-C₃N₄ composites

g-C₃N₄ was prepared according to the paper reported before [25]. 10 g of melamine was put into a porcelain boat with cover, then heated it up from room temperature to 500 °C with the heating rate of 10 °C per minute in the air atmosphere and kept for 2 h. After cooling to room temperature, a canary yellow solid was obtained. Under the similar heating procedures with different pyrolysis temperatures, three copper doped g-C₃N₄ composites were synthesized by employing the crystalline copper chloride [H₂mela]₂[CuCl₅]Cl as precursor. We named these copper doped g-C₃N₄ composites as CuCN-500, CuCN-550 and CuCN-580 for their different pyrolysis temperatures of 500 °C, 550 °C, and 580 °C, respectively. Taking CuCN-500 as an example, detailed synthesis was described as follow: 8.5 g of [H₂mela]₂[CuCl₅]Cl was filled in a porcelain boat with cover, then the precursor was heated from room temperature to 500 °C under the heating rate of 10 °C per minute in air, and kept for 2 h. After the products were naturally cooled to room temperature, a black solid (2.9 g) was obtained. All the flow charts of catalyst preparations were illustrated in Fig. 1. In addition, the pyrolysis of [H₂mela]₂[CuCl₅]Cl under nitrogen atmosphere was also carried out by using the same heating process as CuCN-500. 8.2 g of precursor was added into a porcelain boat with cover and flushed N₂ gas for 30 min to ensure the pure N₂ atmosphere. Then the porcelain was heated up to 500 °C with the heating rate of 10 °C/min and kept for 2 h, 0.8 g of black solid was achieved after cooling to room temperature. The sample was named as CuCN-500-N₂.

By using the same heating process of CuCN-500, a mixture of melamine (5.0 g) and CuCl₂·2H₂O (3.4 g) was ground sufficiently, then the mixture was treated as precursor and pyrolyzed to harvest 2.8 g of black

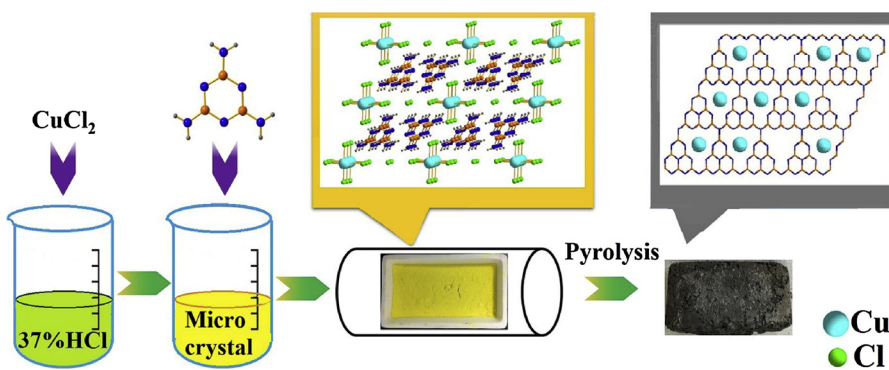


Fig. 1. Synthetic procedure of Cu-g-C₃N₄ composites.

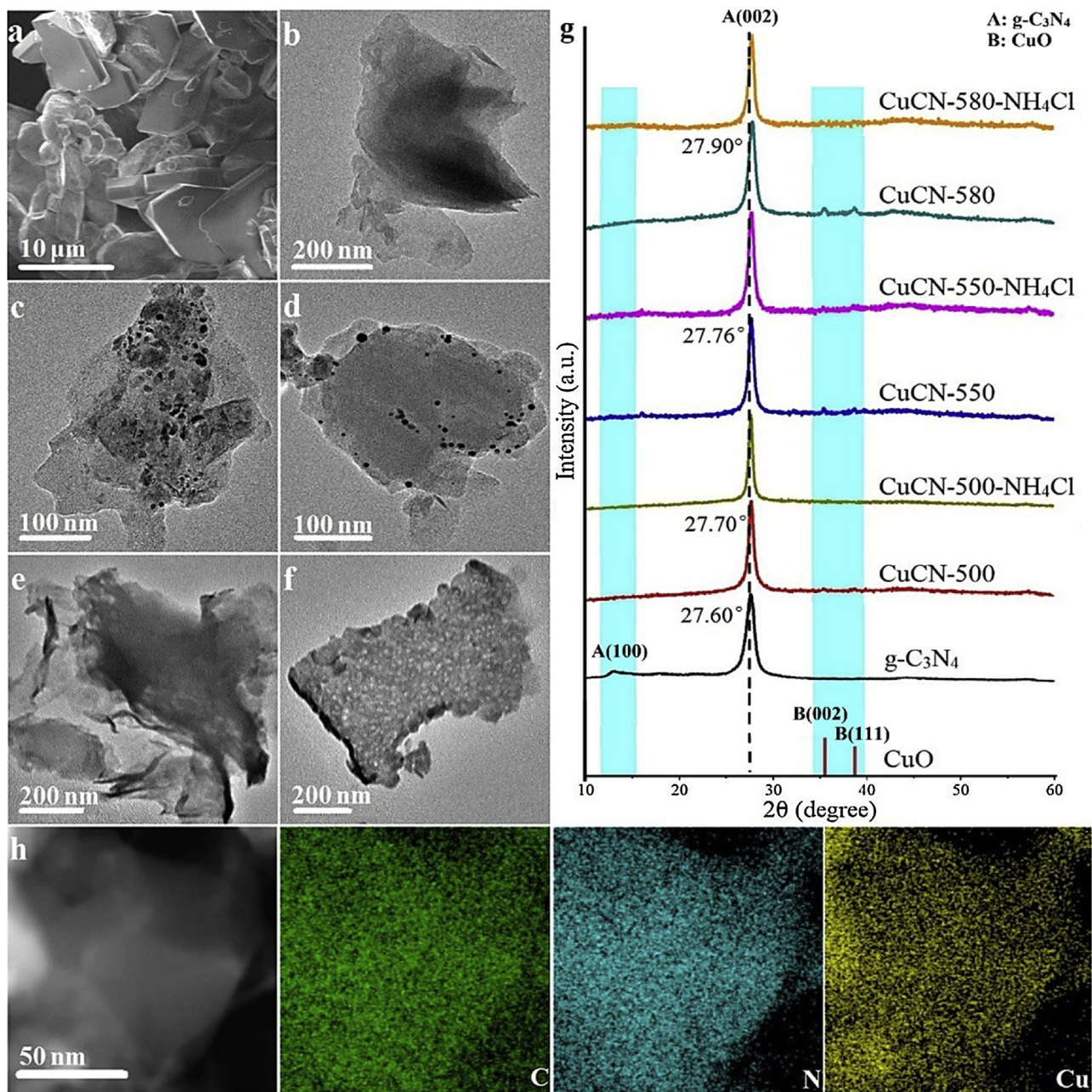


Fig. 2. SEM image of crystalline precursor $[H_2\text{mela}]_2[\text{CuCl}_5]\text{Cl}$ (a); TEM images of CuCN-500 (b), CuCN-550 (c), CuCN-580 (d), CuCN-550-NH₄Cl (e), and CuCN-580-NH₄Cl (f); XRD patterns of Cu-g-C₃N₄ and the corresponding Cu-g-C₃N₄-NH₄Cl composites (g); EDX-elemental mapping images of CuCN-500 for C, N, and Cu (h).

solid products, named as Mela-CuCl₂. Furthermore, we mixed 1.4 g of g-C₃N₄ with 0.6 g of CuCl₂·2H₂O, which was also fully ground and used as precursor. After heating at 500 °C for two hours, 0.25 g of black solid was obtained and named as g-C₃N₄-CuCl₂.

3. Results and discussion

3.1. Catalyst characterization

Through mixing CuCl₂·2H₂O and melamine in hydrochloric acid at room temperature, a mass of yellow powder of the crystalline copper chloride $[H_2\text{mela}]_2[\text{CuCl}_5]\text{Cl}$ was generated quickly. The SEM studies showed that the yellow powder products were regular plate-like microcrystals (Fig. 2a), and its phase purity was confirmed by PXRD (Fig. S1). The structure of this compound is built up by alternate arrangement of negative layers of $[\text{CuCl}_5]^{3n-}$ chains and Cl⁻ anions and

positive layers of doubly protonated melamine cations. Obviously, the protonated melamine ligands act as templates or charge-balancing agents in the architecture, and interact with $[\text{CuCl}_5]^{3n-}$ chains via extensive N-H-Cl hydrogen bonds. Moreover, the highly crystalline quality of this material determines the ordered molecular alignment of melamine ligands and Cu atoms. With the release of Cl⁻ ions in the pyrolysis process, the Cu atoms could directly interact with -NH₂ groups from melamine ligands, leading to the incorporation of Cu atoms in g-C₃N₄ matrix. Thus, this melamine templated crystalline copper chloride is an ideal precursor for synthesizing copper doped g-C₃N₄ composites. Indeed, after heating this precursor at different pyrolysis temperatures in air for two hours, we obtained three Cu-g-C₃N₄ composites, namely, CuCN-500, CuCN-550, and CuCN-580.

The powder XRD patterns of pure g-C₃N₄ and CuCN-500/550/580 were presented in Fig. 2g. In the PXRD patterns of pure g-C₃N₄, the diffraction peak at about 13.20° is assigned to the (100) crystal plane,

which is corresponding to the interplanar separation of tri-s-triazine [32–35]. The diffraction peak at about 27.60° is related to the (002) plane resulted from the stacking of aromatic systems between the carbon nitride layers [33,36,37]. As observed from the PXRD patterns of CuCN-500, CuCN-550, and CuCN-580, their peaks assigned to (002) plane exhibited a right-shift to 27.70°, 27.76°, and 27.90°, respectively, which may be caused by the crystal lattice distortion after Cu chelating [38]. In addition, the disappearances of (100) peak in their PXRD patterns approved the interaction between Cu atoms and tri-s-triazine groups, such variations were consistent with that of other metal doped g-C₃N₄ composites in the reported literature [39]. As displayed in Fig. 2g, there were two weak peaks at around 35.50° and 38.70° in the PXRD patterns of CuCN-500/550/580, indicating the presence of a very small amount of CuO in the pyrolyzed products. It is obvious that the two peaks of CuO increase with the upgrading of pyrolysis temperature, suggesting higher CuO contents in the CuCN-550 and CuCN-580 composites. This result can be ascribed to two reasons: 1) higher pyrolysis temperature may promote the reaction between Cu atoms and oxygen in air; 2) higher pyrolysis temperature provided a favorable crystallization condition for the CuO particles. The TEM images of these Cu-g-C₃N₄ composites showed that they all possessed two-dimensional lamellar structures, however, no CuO nanoparticles were observed in the stacked nanoflakes of CuCN-500 (Fig. 2b), while both CuCN-550 and CuCN-580 contained CuO nanoparticles in their nanoflakes (Fig. 2c and d). The corresponding EDX-elemental mappings revealed the uniform dispersion of C, N, and Cu on the surface of CuCN-500 nanoflake (Fig. 2h). Moreover, by immersing these Cu-g-C₃N₄ composites in an ammonium chloride (NH₄Cl) aqueous solution (1 mol/L) for 24 h, these CuO inclusions can be removed. The NH₄Cl treated samples were named as CuCN-500-NH₄Cl, CuCN-550-NH₄Cl, and CuCN-580-NH₄Cl, respectively. The PXRD patterns of the NH₄Cl treated Cu-g-C₃N₄ composites certified the disappearance of CuO (Fig. 2g). In addition, the TEM images of CuCN-550-NH₄Cl and CuCN-580-NH₄Cl displayed that there were some holes inside the nanoflakes, which may be attributed to the etching of the CuO particles (Fig. 2e and f).

Actually, we have also calcined the [H₂mela]₂[CuCl₅]Cl precursor in a nitrogen atmosphere by using the same heating procedure as CuCN-500, and a black solid was obtained and named as CuCN-500-N₂. Different from CuCN-500, the PXRD patterns of CuCN-500-N₂ suggest the presence of metallic copper in the g-C₃N₄ matrix (Fig. 3a). Furthermore, the TEM image of CuCN-500-N₂ showed that there were plenty of nanoparticles with diameters of ~10 nm in the g-C₃N₄ nanoflakes. According to the information from PXRD, these nanoparticles may be metallic copper. It is clear that the divalent Cu²⁺ ions in [H₂mela]₂[CuCl₅]Cl precursor were reduced to zero valent Cu⁰ atoms under the pyrolysis conditions with the nitrogen atmosphere, while the NH₃ molecules decomposed from melamine may be responsible to the reduction process. Another difference should be noted that the product yield decreased significantly in CuCN-500-N₂ (0.8 g) versus CuCN-500 (2.9 g). Under the synthetic conditions of CuCN-500-N₂, more melamine and its decomposition products were taken away by nitrogen flow, resulting in a low yield of g-C₃N₄ matrix. As a consequence, less Cu atoms coordinated with N atoms from g-C₃N₄, and more reduced Cu⁰ atoms gathered to form nanoparticles.

In order to investigate the superiority of melamine templated crystalline copper chloride [H₂mela]₂[CuCl₅]Cl as precursor for preparing Cu-g-C₃N₄ composites, we used the ground mixture of melamine and CuCl₂·2H₂O as precursor for comparison. The corresponding pyrolyzed product was named as Mela-CuCl₂. Its PXRD data was shown in Fig. 3b, besides the g-C₃N₄, Mela-CuCl₂ contained several copper compounds, including Cu₃N, CuO, Cuprite (PDF05-0667) and metallic copper. Since the precursor of Mela-CuCl₂ was prepared by grinding melamine and CuCl₂·2H₂O, the inorganic species and melamine ligands were integrated at micro-scale. When heating this material in air, the large CuCl₂·2H₂O particles could not only react with melamine or its decomposed species, but also react with O₂ from air, and thus leading to

the complex components of Mela-CuCl₂. Its TEM image also showed that different nanoparticles and nanosheets were mixed with g-C₃N₄ (Fig. 3e). We have also calcined the ground mixture of g-C₃N₄ and CuCl₂·2H₂O by using the same pyrolysis conditions of CuCN-500, and the corresponding product was named as g-C₃N₄-CuCl₂. However, PXRD studies indicated that only CuO existed in the samples of g-C₃N₄-CuCl₂ (Fig. 3c), and SEM image showed its micro-crystalline grain morphology (Fig. 3f). Concluding from these results, we could note that the ordered molecular alignment of melamine ligands and Cu atoms in [H₂mela]₂[CuCl₅]Cl is crucial to the preparation of high dispersed Cu-g-C₃N₄ composites.

Cu-g-C₃N₄ composites and g-C₃N₄ were characterized by FTIR. As shown in Fig. 4, for g-C₃N₄, two broad bands centered at 3138 and 3401 cm⁻¹ are originated from the symmetric and asymmetric stretching modes of amino groups, respectively [40,41]. These strong absorption peaks indicated that there are plenty of terminal amino groups located at the defect sites or the surfaces of the as-prepared g-C₃N₄. However, in the FTIR spectra of Cu-g-C₃N₄ composites, the bands at 3138 and 3401 cm⁻¹ display much weaker absorptions, suggesting less terminal amino groups resided in the samples of Cu-g-C₃N₄ composites [42,43]. Clearly, g-C₃N₄ and Cu-g-C₃N₄ composites contained different amounts of -NH_x (x = 1, 2) groups, this difference was further proved by XPS studies discussed below. The bands in the region of 1200–1700 cm⁻¹ dominate the spectra of g-C₃N₄ and Cu-g-C₃N₄ composites with striking maxima at 1630, 1460, 1408, 1328, 1243 cm⁻¹ and shoulder at 1152 cm⁻¹. These absorption bands exhibited the similar features of g-C₃N₄ materials reported before: 1) the bands of 1630, 1460, 1328, 1243 and 1152 cm⁻¹ can be ascribed to the skeletal vibrations of heptazine heterocyclic ring (C₆N₇) [40,44–46]; 2) the peak at 1408 cm⁻¹ may derive from the stretching vibrations of triazine ring (C₃N₃) [40,44]. Nevertheless, the absorption intensity of Cu-g-C₃N₄ composites in this region (1200–1700 cm⁻¹) was much lower compared with that of g-C₃N₄. This difference may be attributed to the Cu-N_x species formed in the Cu-g-C₃N₄ composites, since the coordination between Cu atoms and N atoms could reduce the skeletal or stretching vibrations of heptazine or triazine rings [46]. Similar trend has also been found for the peak at 809 cm⁻¹, which belongs to an out-of-plane vibration characteristic of both s-triazine and heptazine ring systems [38,40,44,47,48]. These results demonstrated that incorporating Cu atoms in the polymerization process of melamine restrained the remains of uncondensed amino groups, whilst the Cu-N_x species were formed by coordinating Cu atoms with the N atoms from heptazine or triazine rings.

To investigate the element states and chemical bonds on the surface of g-C₃N₄ and Cu-g-C₃N₄ composites, their corresponding XPS spectra were analyzed. As shown in Fig. 5a, the N 1s XPS spectra of g-C₃N₄ can be divided into three peaks of 398.6 eV, 399.3 eV, and 400.8 eV. The main peak at 398.6 eV was assigned to the sp²-hybridized N atoms in the C = N–C bonds of triazine rings. The peak at 399.3 eV can be ascribed to the sp³-hybridized N atoms in the N–(C)₃ group [49–51]. The existence of these two peaks confirmed the generation of g-C₃N₄, while the peak at 400.8 eV was attributed to the amino N–H_x groups caused by incomplete condensation [49]. In addition, a small peak with binding energy of 404.5 eV was identified as the charging effect or π excitation of the –C≡N groups and heterocycles [46]. However, in the N 1s spectra of CuCN-500 (Fig. 5b), its binding energy of C = N–C groups increased to 399.0 eV compared with that of g-C₃N₄ at 398.6 eV, whilst the peaks of N–(C)₃ and amino N–H_x groups in CuCN-500 exhibited the same trend and shifted to higher binding energy of 400.1 eV and 401.2 eV, respectively. Comparing the N–H_x signal of CuCN-500 to g-C₃N₄, it is obvious that the content of N–H_x groups in CuCN-500 is lower than that of g-C₃N₄, which has been further evidenced by FTIR discussed above. This difference was also observed in the N 1s XPS spectra of CuCN-550 and CuCN-580. All these results indicated that extensive Cu–N bonds were formed in the Cu-g-C₃N₄ composites [52–55]. Moreover, by contrast with g-C₃N₄ containing 52.9% of

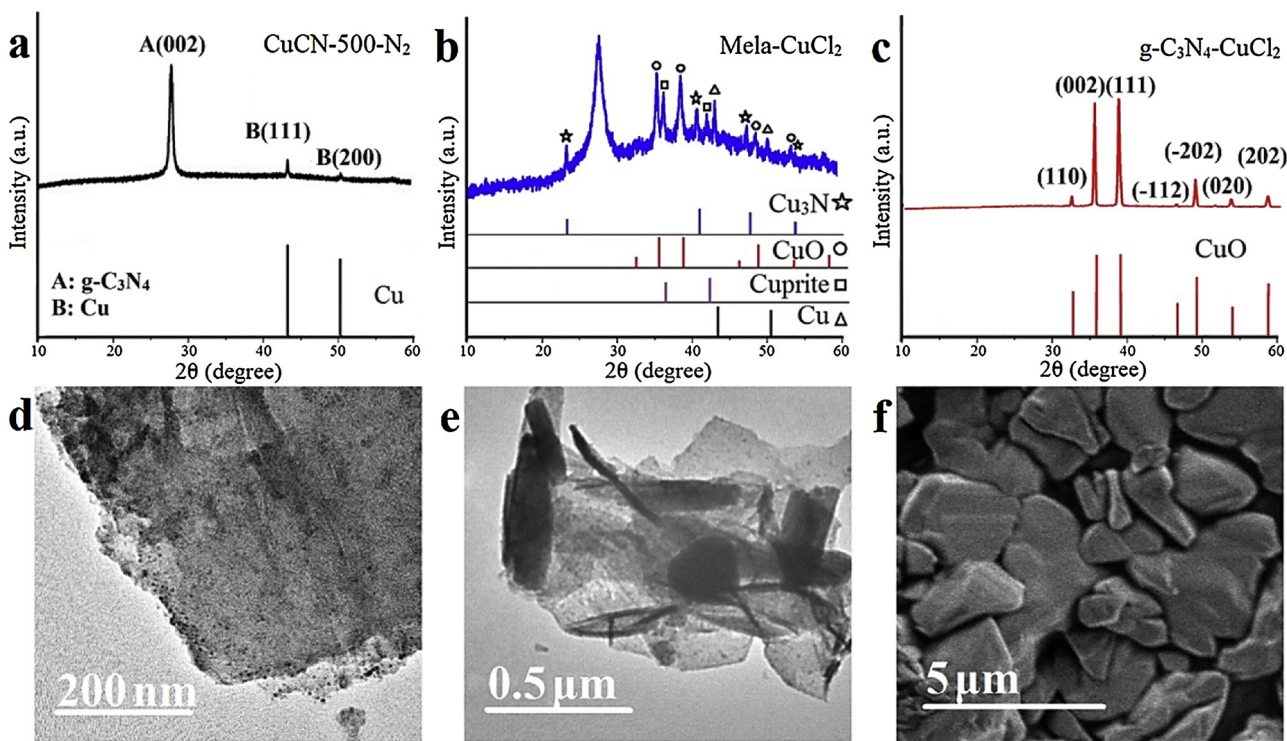


Fig. 3. XRD patterns of CuCN-500-N₂ (a), Mela-CuCl₂ (b), and g-C₃N₄-CuCl₂ (c); TEM images of CuCN-500-N₂ (d), and Mela-CuCl₂ (e); SEM image of g-C₃N₄-CuCl₂ (f).

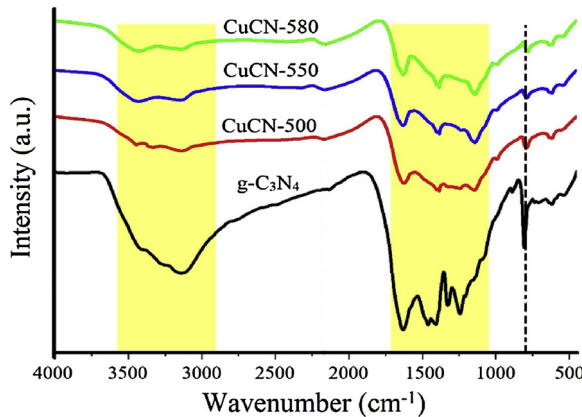


Fig. 4. FTIR Spectra of Cu-g-C₃N₄ composites and pure g-C₃N₄.

pyridinic N, introducing Cu atoms in the polymerization led to a higher content (67.3%) of pyridinic N in CuCN-500. As shown in Fig. 5c and d, CuCN-550 and CuCN-580 owned more pyridinic N atoms in comparison with CuCN-500, which may be related to their higher pyrolysis temperature, since higher temperature is benefit for the complete condensation of melamine.

The Cu 2p XPS spectra of Cu-g-C₃N₄ composites were tested. Taking CuCN-500 as an example (Fig. 5e), the peak located at 932.7 eV corresponds to the reductive state [56], while the auger kinetic energy at 571.2 eV further approved the existence of Cu⁺ ions instead of metallic copper (Fig. 5f) [56]. The binding energy at 935.1 eV was ascribed to oxidation state of copper species and the obvious satellite peak at 943.3 eV provided a powerful proof of Cu²⁺ ions [57–59]. From the PXRD of CuCN-500, no diffraction peaks of Cu₂O were found so that the Cu⁺ ions might be embedded and stabilized in g-C₃N₄ through coordinating with N atoms. We can also conclude from PXRD that only a small amount of Cu²⁺ ions are in the form of CuO. However, the Cu 2p_{2/3} energy position (933.3 eV) of pure CuO is lower than the data

obtained in this work [38,60], suggesting most of Cu²⁺ ions coordinate with N atoms from g-C₃N₄. In order to further certify the incorporation of Cu²⁺ ions in g-C₃N₄, after immersing the samples in NH₄Cl aqueous solution to remove the CuO components, the Cu 2p XPS spectra of NH₄Cl treated CuCN-500 still owned the Cu 2p_{2/3} binding energy at 932.4 eV along with the satellite peak at 942.3 eV (Fig. 5g), and the above results were further proved by auger electron spectrum (Fig. 5h). Thus, the data displayed above confirmed the co-existence of Cu⁺ and Cu²⁺ ions in CuCN-500. As shown in Fig. S7, similarly to CuCN-500, both CuCN-550 and CuCN-580 contain Cu⁺ and Cu²⁺ ions in g-C₃N₄ matrix. ICP-AES analyses have been used to test the content of Cu in the catalysts. The contents of Cu in the samples of CuCN-500, CuCN-550, and CuCN-580 are 25.9, 20.9, and 17.1 wt %, respectively.

3.2. Catalytic performance

Typical organic dye pollutants (RhB, MB, and MO) were chosen to evaluate the catalytic activities of these Cu-g-C₃N₄ composites. All the degradation processes were performed in a dark environment, and the solutions were kept at neutral pH condition. Before adding H₂O₂ in the catalytic system, the mixture of Cu-g-C₃N₄ composites and organic dye aqueous solution was stirred for 30 min. to reach the equilibrium of adsorption-desorption, where the concentration of organic dye kept constant over a period of time. As shown in Fig. 6a–c, all these Cu-g-C₃N₄ composites displayed excellent degradation performances toward RhB, MB, and MO. By contrast with CuCN-500, CuCN-550 and CuCN-580 exhibited relatively low catalytic activities for the degradation of organic dyes. This difference may be attributed to the higher CuO contents in the samples of CuCN-550 and CuCN-580, while the CuO inclusions played a limited role in the degradation process. Hence, more Cu-N_x active sites in CuCN-500 could offer higher catalytic efficiency to produce hydroxyl radicals. Similar reactions have been carried out for CuO and g-C₃N₄ in darkness, and their low degradation abilities were clarified. As illustrated in Fig. 6a–c, CuCN-500 could remove 92.3% of RhB and 100% of MB within 15 min. By comparison, only 11.1% of RhB and 6.0% of MB were removed by CuO, 18.2% of RhB and 16.1% of MB

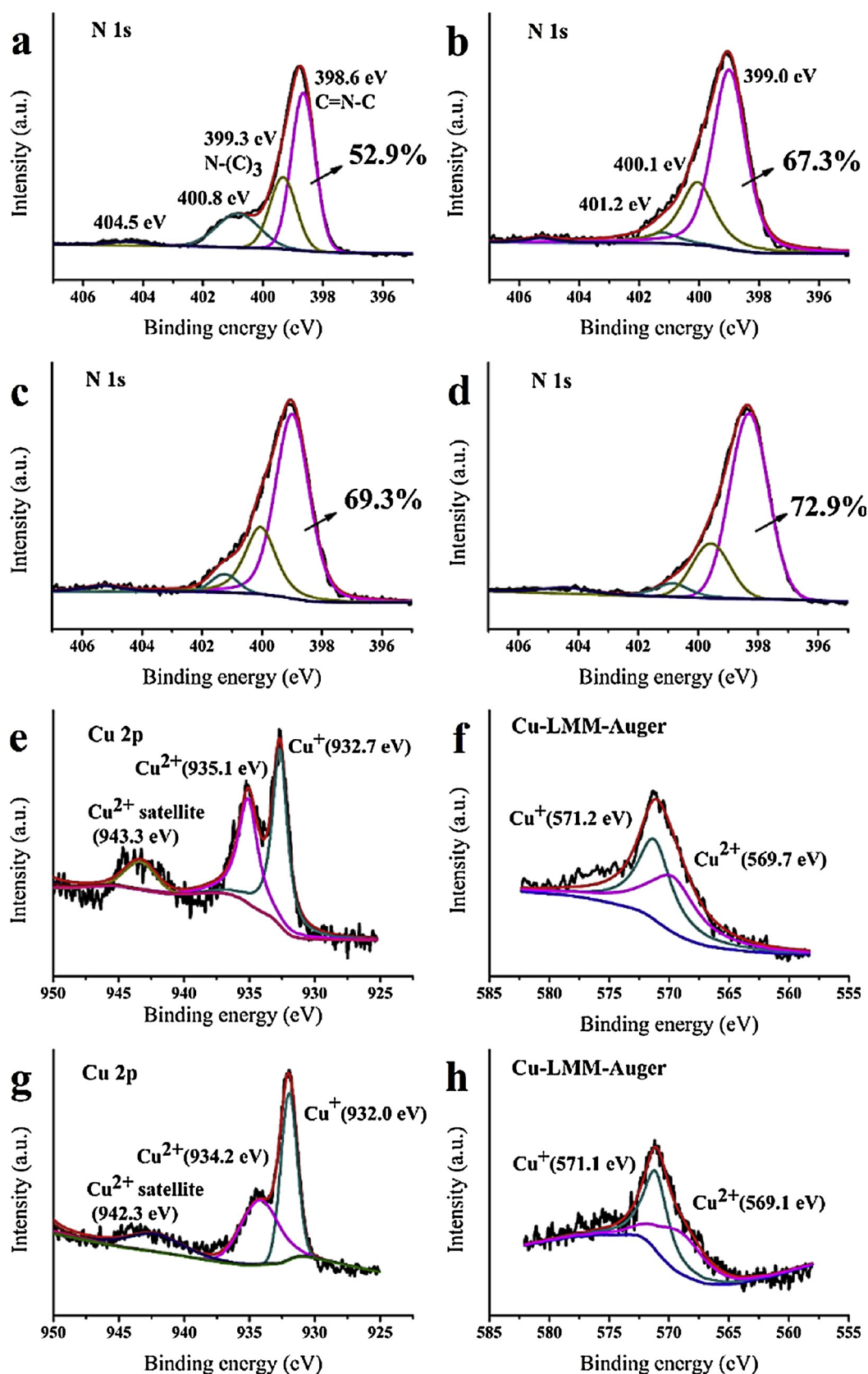


Fig. 5. XPS spectra of N 1s for g-C₃N₄ (a), CuCN-500 (b), CuCN-550 (c), and CuCN-580 (d); XPS spectra of Cu 2p for CuCN-500 (e) and CuCN-500-NH₄Cl (g); Cu Auger Electron (LMM) spectra of CuCN-500 (f) and CuCN-500-NH₄Cl (h).

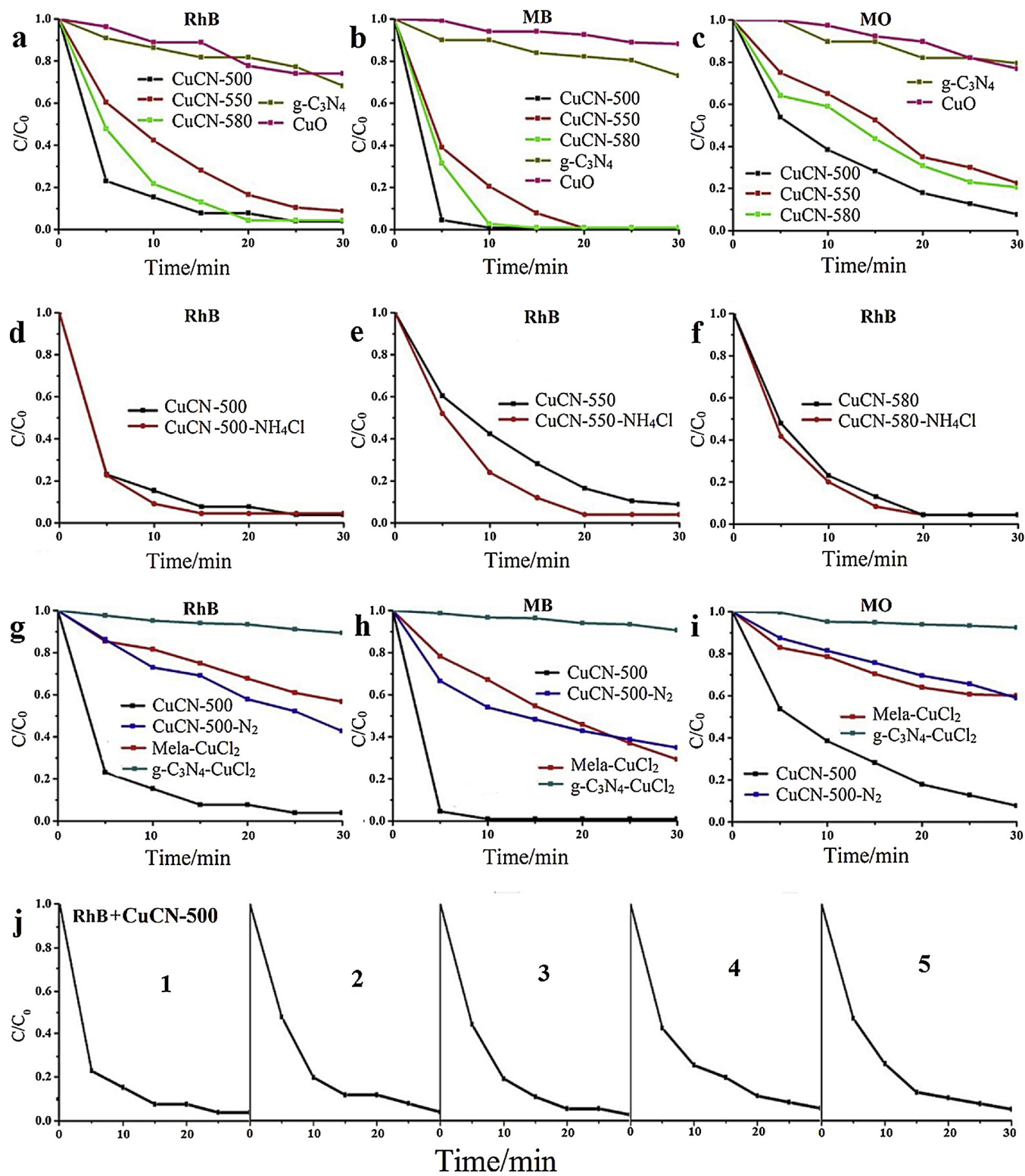


Fig. 6. Degradation performances of different catalysts for RhB (a), MB (b), and MO (c); (d-f) removal efficiency of RhB by using Cu-g-C₃N₄ and corresponding NH₄Cl treated composites; degradation performances of CuCN-500, CuCN-500-N₂, Mela-CuCl₂, and g-C₃N₄-CuCl₂ for RhB (g), MB (h), and MO (i); (j) cyclic experiments of CuCN-500 for degrading RhB.

were removed by g-C₃N₄ in 15 min. The MO removal rate by CuCN-500 reached up to 92.4% in 30 min., while for CuO and g-C₃N₄, their removal rates of MO within 30 min. were 23.1% and 20.5%, respectively. TOC removal efficiency of CuCN-500 for RhB and MB was tested. The removal efficiency of TOC in RhB aqueous solution was 42% (catalyst: 0.2 g/L, 60 min), and in MB aqueous solution was 75% (catalyst: 1 g/L,

120 min). Obviously, the Cu-N_x species of Cu-g-C₃N₄ composites played a dominate role in the degradation of organic dyes. Further verifications were taken by testing the degradation abilities of the NH₄Cl treated Cu-g-C₃N₄ composites.

The CuO inclusions in the samples of Cu-g-C₃N₄ composites were eliminated by immersing the samples in an ammonium chloride

Table 1

Comparison of the catalytic activities of CuCN-500 with other Fenton-like catalysts reported in literature.

catalysts	organics	m_{Cat} (g/L)	C_{Org} (ppm)	$C_{\text{H}_2\text{O}_2}$ (mM)	t (min)	Conversion (%)	ref
10%Fe-g-C ₃ N ₄	MB	0.5	50	400	30	100	[61]
Fe-g-C ₃ N ₄ /GMC	RhB	0.8	50	40	40	95	[62]
Cu-Al ₂ O ₃ -4.5wt%g-C ₃ N ₄	RhB	0.5	10	12.5	10	45	[57]
Fe/MnO ₂	MB	0.5	100	1647	120	94	[63]
5Cu/Al ₂ O ₃ -750	RhB	1	10	1000	30	95	[64]
CuCN-500	RhB	0.2	10	300	15	92	This work
CuCN-500	MB	0.2	10	300	15	100	This work
CuCN-500	MO	0.2	10	300	30	92	This work
CuCN-500	4-NP	1	10	300	60	100	This work
CuCN-500	BPA	1	10	300	60	96	This work
CuCN-500	TC	0.2	10	300	30	100	This work

aqueous solution (1 mol/L) for 24 h, the phase purities of the NH₄Cl treated Cu-g-C₃N₄ composites were confirmed by PXRD (Fig. 2g). Compared with the original Cu-g-C₃N₄ composites, the NH₄Cl treated catalysts showed slightly higher catalytic activities for degrading RhB (Fig. 6d-f). Since only a small amount of CuO inclusions were embedded in the Cu-g-C₃N₄ nanoflakes, eliminating CuO could just increase limited Cu-N_x species to a unit mass of catalyst. Therefore, high density Cu-N_x species in the Cu-g-C₃N₄ composites were responsible for their enhanced catalytic capacities. Compared with other Fenton-like catalysts reported in literature (Table 1), CuCN-500 exhibited excellent catalytic activity for degrading organic dyes.

In addition to organic dyes, we have investigated the catalytic performance of CuCN-500 for another three types of pollutants, including Tetracycline (TC), 4-Nitrophenol (4-NP), and Bisphenol A (BPA). As shown in Fig. S10, CuCN-500 could remove 100% of TC in 30 min, 100% of 4-NP and 96% of BPA in 60 min. These results suggest that CuCN-500 could be used to degrade other types of pollutants besides organic dyes. The detailed catalytic activities of CuCN-500 for these pollutants have been summarized in Table 1.

Compared with CuCN-500, CuCN-500-N₂, Mela-CuCl₂, and g-C₃N₄-CuCl₂ all showed relatively low catalytic activities for the degradation of organic dyes (Fig. 6g-i). Within 15 min., only 30.8% of RhB and 51.6% of MB were removed by CuCN-500-N₂, 25.0% of RhB and 45.4% of MB were removed by Mela-CuCl₂. While for the degradation of MO, the removal rates of CuCN-500-N₂ and Mela-CuCl₂ within 30 min. were 41.0% and 39.5%, respectively. Since g-C₃N₄-CuCl₂ contained only micro-crystalline CuO, its degradation performances toward organic dyes were comparable with that of the commercial CuO described above. Due to the advantage of [H₂mela]₂[CuCl₅]Cl with highly ordered molecular alignment, CuCN-500 exhibited the best catalytic activity among these materials, which was originated from its high content of Cu-N_x species.

A previous Cu-doped-g-C₃N₄ composite prepared from Cu-melamine supramolecular network exhibited efficient visible light photocatalytic activity for degrading methylene blue (MB) [65]. According to its' photocatalytic experiments, a solution of catalyst, MB, and H₂O₂ was stirred in darkness for 40 min., and then the solution was irradiated by visible light. Clearly, this catalytic process started from the visible light irradiation, which was not a Fenton-like reaction. The photocatalytic ability of this Cu-doped-g-C₃N₄ composite is highly dependent on g-C₃N₄, which generates photo-excited electron – hole pairs. On the contrary, the Cu-g-C₃N₄ composites prepared in the present work act as heterogeneous Fenton-like catalysts for the degradation of organic dyes. The function of g-C₃N₄ is more like a matrix to encapsulate Cu²⁺ ions. We have tested the degradation performance of CuCN-500 for RhB with addition of H₂O₂ under dark condition and visible light irradiation. As shown in Fig. S11, the degradation rates of RhB in darkness and visible light are nearly the same, indicating that visible light irradiation has no effect on the catalytic process.

Control experiments have been carried out by adding CuCN-500 and RhB without H₂O₂, RhB and H₂O₂ without catalyst, and only RhB in the

reactions. As shown in Fig. S8, only adding CuCN-500 and RhB in the reactions could not degrade RhB. Similarly, no degradation was occurred in the case of only adding RhB in water. In the reaction mixture of RhB and H₂O₂, H₂O₂ exhibit inefficient degradation ability for oxidizing RhB. These control experiments demonstrate that CuCN-500 could not degrade organic dyes without addition of H₂O₂ and the utilization efficiency of H₂O₂ is very low without addition of CuCN-500. Thus, reaction mixture of CuCN-500 and H₂O₂ is preferable to produce hydroxyl radicals, which can effectively degrade organic dyes.

We have investigated the formation of Cu²⁺/Cu⁺ and NO₃⁻ ions for CuCN-500 during the degradation of RhB with addition of H₂O₂. ICP-MS was used to detect the leaching of copper from CuCN-500 in the reaction solution. As shown in Fig. 7a, the concentration of leached copper was 0.0061 mM after 90 min. reaction, suggesting that only trace amount of Cu-N_x species were oxidized. Ion Chromatograph was used to analyze the concentration of NO₃⁻ ions in the reaction solution (Fig. 7a). After 90 min. reaction, the concentration of NO₃⁻ ions was 0.036 mM. Obviously, the concentration of NO₃⁻ ions was much higher than that of Cu²⁺ ions in the reaction solution. These results indicated that most of NO₃⁻ ions may be generated from the oxidation of the -NH_x groups in g-C₃N₄ matrix, which were produced by incomplete condensation of melamine. Various active oxygen species may oxidize the -NH_x groups to NO₃⁻ ions during the reaction.

The stability of CuCN-500 was investigated. Cyclic experiments were carried out under the same conditions for the degradation of RhB, and the catalyst was washed with deionized water and anhydrous ethanol after one cycle for the next run. As observed in Fig. 6j, the catalytic activity of CuCN-500 showed only a slight decrease after 5 cycles, indicating its good stability and repeatability. XRD spectra of CuCN-500 used for 5 cycles still showed a strong main peak at 27.70° (Fig. 7b), approving the intact skeleton of g-C₃N₄. Furthermore, FTIR of CuCN-500 used for 5 cycles also proved that the g-C₃N₄ remained intact (Fig. 7c). The bands of 1630, 1460 and 1243 cm⁻¹ can be ascribed to the skeletal vibrations of heptazine heterocyclic ring (C₆N₇). The absorption intensity of the used sample in the region of 1200-1700 cm⁻¹ was still much lower than that of pure g-C₃N₄, which meant the Cu-N_x species remained in the Cu-g-C₃N₄ composite. However, after 5 cycle reactions, the peak at 3439 cm⁻¹ which assigned to -OH group was significantly enhanced. This difference may be caused by the oxidation of -NH_x groups on the surface of g-C₃N₄ during the reaction. The Cu 2p XPS spectra of the fresh-prepared CuCN-500 and CuCN-500 used for 5 cycles did not show much difference (Fig. 7d), except that the used sample contained more divalent Cu²⁺ ions than monovalent Cu⁺ ions. The increased content of Cu²⁺ ions may be ascribed to the oxidizing environment of the catalytic process.

In order to explore the surface reaction process of CuCN-500, the catalyst stirred in RhB aqueous solution under the different reaction time was collected and dried for the FTIR measurement. As shown in Fig. 8a-b, (I) the fresh catalyst showed a wide absorption band at 3446 cm⁻¹, which can be ascribed to the telescopic vibrations of -OH. (II) After adsorbing RhB for 30 min in darkness, the band of -OH

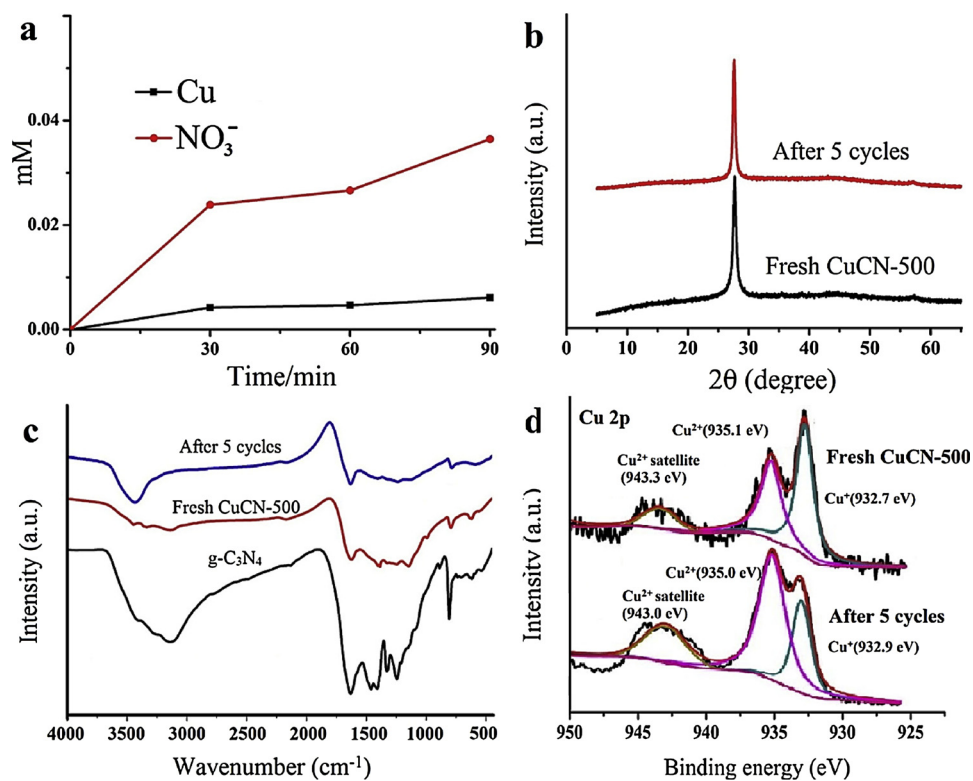


Fig. 7. (a) Time-concentration profiles of Cu and NO_3^- dissolved out from CuCN-500; XRD (b) and FTIR (c) spectra of fresh-prepared CuCN-500 and the corresponding sample after five reaction cycles; (d) XPS spectra of Cu 2p for CuCN-500 and CuCN-500 used for 5 cycles.

shifted to lower wavenumber (3435cm^{-1}). The decreased wavenumber of $-\text{OH}$ group indicated that some RhB molecules interacted with electron-rich $-\text{OH}$ groups on the surface of catalyst [66,67]. After adding H_2O_2 for 5 (III) and 10 min. (IV), the band of $-\text{OH}$ group showed no shift at 3435cm^{-1} and 3434cm^{-1} , respectively. After stirring with H_2O_2 for 20 min. (V), most of RhB molecules were removed, however, the absorption band of $-\text{OH}$ group still located at 3435cm^{-1} . This change suggested that some small organic molecules were attached on the surface of $\text{g-C}_3\text{N}_4$, which may lead to a slight decline of its catalytic activity after the first cycle in the cycle experiments (Fig. 6j).

To figure out the chief active oxygen species taken part in the degradation of RhB, isopropanol (IPA) was chosen as hydroxyl radical trapping scavenger. We have tested the effect of isopropanol (IPA) concentration (0.1 M–0.7 M) on degradation of RhB by CuCN-500. As shown in Fig. 8c, when the concentration of IPA was 0.1 M, the degradation rate of RhB decreased remarkably in comparison with the original degradation curve. This result demonstrated that hydroxyl radicals are crucial to the degradation of RhB. When increasing the concentration of IPA from 0.1 to 0.7 M, the degradation rate of RhB displayed a continued decline. However, the degradation rate of RhB exhibited no big change with the concentration of IPA increased from 0.5 to 0.7 M, indicating that most of the as-produced hydroxyl radicals have been captured by IPA. Although the degradation rate decreased, there was still a portion of RhB that were degraded in the presence of IPA. Obviously, there were other active oxygen species that affected the degradation process.

DMPO-trapping EPR spectra of CuCN-500, CuCN-550, CuCN-580, and their corresponding NH_4Cl treated samples all exhibit 4-fold peaks with an intensity ratio of 1:2:2:1, which can be assigned to the typical DMPO- OH (Fig. 8d) [62,68]. Furthermore, we have applied EPR spin-trapping technique to perform the quantitative experiment of hydroxyl radicals for CuCN-500, CuCN-550, CuCN-580, and their corresponding NH_4Cl treated samples with addition of H_2O_2 (Fig. 8d). DPPH (1,1-

diphenyl-2-picrylhydrazyl, 1 mM) was used as standard for the quantitative experiment of hydroxyl radicals, and DMPO was employed as capture agent. By comparing the peak area of radicals produced by standard product with that of all the catalysts, the amount of hydroxyl radicals produced by the catalysts can be calculated, and the results were summarized as follows: CuCN-500, 7.092×10^{-3} mM; CuCN-500- NH_4Cl , 7.569×10^{-3} mM; CuCN-550, 5.028×10^{-3} mM; CuCN-550- NH_4Cl , 5.472×10^{-3} mM; CuCN-580, 5.982×10^{-3} mM; CuCN-580- NH_4Cl , 6.347×10^{-3} mM. These results show that the concentrations of hydroxyl radicals produced by the catalysts are in accordance with their degradation performances. Compared with Cu- $\text{g-C}_3\text{N}_4$, NH_4Cl treated Cu- $\text{g-C}_3\text{N}_4$ composites without CuO inclusions produce more hydroxyl radicals. This finding further proves that the Cu- N_x species play a key role in producing hydroxyl radicals from H_2O_2 . Thus, CuCN-500 with higher content of Cu- N_x species generates more hydroxyl radicals than CuCN-550 and CuCN-580.

The roles of superoxide radical (O_2^-) and singlet oxygen (${}^1\text{O}_2$) in the reactions have been investigated. EPR spin-trapping technique was used to detect O_2^- and ${}^1\text{O}_2$ in the reaction systems of CuCN-500, CuCN-550, CuCN-580, and their corresponding NH_4Cl treated samples with addition of H_2O_2 . 5, 5-dimethyl-pyrroline N-oxide (DMPO) was chosen to trap O_2^- in methanol solution, while 2,2,6,6-tetramethyl-4-Piperidinol (TEMP) was employed to trap ${}^1\text{O}_2$ in aqueous solution. As shown in Fig. 8e, DMPO-trapping EPR spectra of all catalysts displayed six-line signals, which were the characteristic peaks of O_2^- . Similarly, TEMP-trapping EPR spectra of all catalysts exhibited 1:1:1 triplet signals, which were the characteristic peaks of ${}^1\text{O}_2$ (Fig. 8f). Thus, besides hydroxyl radicals, superoxide radical and singlet oxygen were generated in the Fenton reactions of all catalysts, where these radicals took part in the degradation process.

4. Conclusions

Three copper doped $\text{g-C}_3\text{N}_4$ composites were successfully

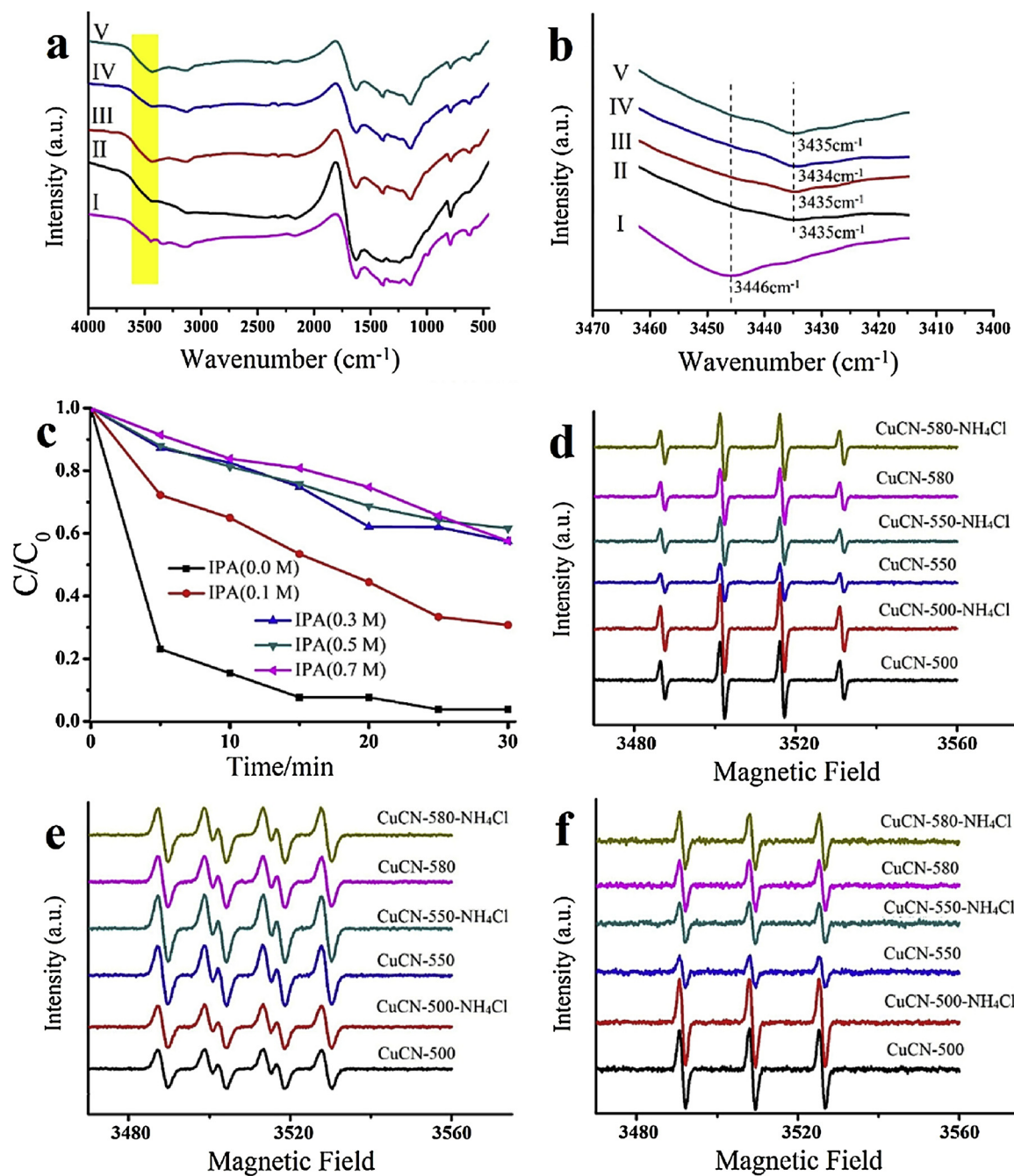


Fig. 8. (a) FTIR spectra of various samples: (I) fresh-prepared CuCN-500; (II) CuCN-500 adsorbed RhB for 30 min; CuCN-500 reacted with RhB after adding H_2O_2 for 5 min. (III), 10 min. (IV), and 20 min. (V). (b) FTIR spectra of various samples in the range of 3420-3470 cm^{-1} . (c) Degradation performance of CuCN-500 for RhB by adding isopropanol with different concentrations. DMPO spin-trapping EPR spectra for $\cdot\text{OH}$ (d) and $\cdot\text{O}_2$ (e) in the aqueous and methanol solutions of $\text{Cu-g-C}_3\text{N}_4$ and their corresponding NH_4Cl treated samples with H_2O_2 , respectively. (f) TEMP spin-trapping EPR spectra for $\cdot\text{O}_2$ in the aqueous solutions of $\text{Cu-g-C}_3\text{N}_4$ and their corresponding NH_4Cl treated samples with H_2O_2 .

synthesized by pyrolyzing melamine templated crystalline copper chloride $[\text{H}_2\text{mela}]_2[\text{CuCl}_5]\text{Cl}$ at different temperature. In contrast to the physical mixing precursors ($\text{CuCl}_2\&\text{mela}$ and $\text{CuCl}_2\&\text{g-C}_3\text{N}_4$), $[\text{H}_2\text{mela}]_2[\text{CuCl}_5]\text{Cl}$ possessed highly ordered molecular arrangement of melamine ligands and Cu atoms, which was benefit for harvesting high content of Cu-N_x species in the pyrolysis process. The as-formed Cu-N_x species were well dispersed in the $\text{g-C}_3\text{N}_4$ matrix, which was approved by TEM, EDS mapping, FTIR, and XPS. Due to the strong catalytic activity of Cu-N_x species for producing hydroxyl radicals from H_2O_2 at neutral pH, these $\text{Cu-g-C}_3\text{N}_4$ composites can be used as promising heterogeneous Fenton-like catalysts for the degradation of

typical organic dye pollutants, including RhB, MB, and MO. However, the catalysts prepared from physical mixing precursors of mela/ $\text{g-C}_3\text{N}_4$ and CuCl_2 contained less Cu-N_x species, and thus exhibited much lower degradation performance. Among these materials, CuCN-500 owned the best catalytic activity and good stability, which could be selected as a potential catalyst in the practical wastewater treatment. Our research proved that melamine templated crystalline copper chlorides can be used as efficient precursors for preparing heterogeneous Fenton-like catalysts with high catalytic activity.

Acknowledgements

W.X acknowledges financial support from National Natural Science Foundation of China (21571102, 21705081), the Natural Science Foundation of Jiangsu Province (BK20150949, BK20161037), the Jiangsu Specially-Appointed Professor, "High-Level Talents in Six Industries" of Jiangsu Province (XCL-040).

Appendix A. Supplementary data

Supplementary material related to this article can be found, in the online version, at doi:<https://doi.org/10.1016/j.apcatb.2019.117830>.

References

- [1] S.A. Hassanzadeh-Tabrizi, M.M. Motlagh, S. Salahshour, Synthesis of ZnO/CuO nanocomposite immobilized on gamma-Al₂O₃ and application for removal of methyl orange, *Appl. Surf. Sci.* 384 (2016) 237–243.
- [2] C. Leal Marchena, L. Lerici, S. Renzini, L. Pierella, L. Pizzio, Synthesis and characterization of a novel tungstosilicic acid immobilized on zeolites catalyst for the photodegradation of methyl orange, *Appl. Catal. B: Environ.* 188 (2016) 23–30.
- [3] C.H. Choi, D.H. Ko, B. Park, Y. Choi, W. Choi, D.P. Kim, Air-water interfacial fluidic sonolysis in superhydrophobic silicon-nanowire-embedded system for fast water treatment, *Chem. Eng. J.* 358 (2019) 1594–1600.
- [4] P. Wang, X. Wang, S. Yu, Y. Zou, J. Wang, Z. Chen, N.S. Alharbi, A. Alsaedi, T. Hayat, Y. Chen, X. Wang, Silica coated Fe₃O₄ magnetic nanospheres for high removal of organic pollutants from wastewater, *Chem. Eng. J.* 306 (2016) 280–288.
- [5] A.-K. Ghattas, F. Fischer, A. Wick, T.A. Ternes, Anaerobic biodegradation of (emerging) organic contaminants in the aquatic environment, *Water Res.* 116 (2017) 268–295.
- [6] I. Oller, S. Malato, J.A. Sanchez-Perez, Combination of advanced oxidation processes and biological treatments for wastewater decontamination-A review, *Sci. Total Environ.* 409 (2011) 4141–4166.
- [7] S. Zhao, H. Zhu, Z. Wang, P. Song, M. Ban, X. Song, A loose hybrid nanofiltration membrane fabricated via chelating-assisted in-situ growth of Co/Ni LDHs for dye wastewater treatment, *Chem. Eng. J.* 353 (2018) 460–471.
- [8] M.A. Oturan, J.J. Aaron, Advanced oxidation processes in water/wastewater treatment: principles and applications, A review, *Crit. Rev. Environ. Sci. Technol.* 44 (2014) 2577–2641.
- [9] I. Michael, L. Rizzo, C.S. McArdell, C.M. Manaia, C. Merlin, T. Schwartz, C. Dagot, D. Fatta-Kassinos, Urban wastewater treatment plants as hotspots for the release of antibiotics in the environment: a review, *Water Res.* 47 (2013) 957–995.
- [10] N.N. Mahamuni, Y.G. Adegbola, Advanced oxidation processes (AOPs) involving ultrasound for waste water treatment: a review with emphasis on cost estimation, *Ultrason. Sonochem.* 17 (2010) 990–1003.
- [11] H. Kim, J. Lim, S. Lee, H.H. Kim, C. Lee, J. Lee, W. Choi, Spontaneous generation of H₂O₂ and hydroxyl radical through O₂ reduction on copper phosphide under ambient aqueous condition, *Environ. Sci. Technol.* 53 (2019) 2918–2925.
- [12] M. Hartmann, S. Kullmann, H. Keller, Wastewater treatment with heterogeneous Fenton-type catalysts based on porous materials, *J. Mater. Chem.* 20 (2010) 9002–9017.
- [13] Y. Yang, C. Zhang, D. Huang, G. Zeng, J. Huang, C. Lai, C. Zhou, W. Wang, H. Guo, W. Xue, R. Deng, M. Cheng, W. Xiong, Boron nitride quantum dots decorated ultrathin porous g-C₃N₄: Intensified exciton dissociation and charge transfer for promoting visible-light-driven molecular oxygen activation, *Appl. Catal. B: Environ.* 245 (2019) 87–99.
- [14] Y. Yang, C. Zhang, C. Lai, G. Zeng, D. Huang, M. Cheng, J. Wang, F. Chen, C. Zhou, W. Xiong, BiOX (X = Cl, Br, I) photocatalytic nanomaterials: Applications for fuels and environmental management, *Adv. Colloid Interface Sci.* 254 (2018) 76–93.
- [15] C. Zhou, P. Xu, C. Lai, C. Zhang, G. Zeng, D. Huang, M. Cheng, L. Hu, W. Xiong, X. Wen, L. Qin, J. Yuan, W. Wang, Rational design of graphic carbon nitride copolymers by molecular doping for visible-light-driven degradation of aqueous sulfamethazine and hydrogen evolution, *Chem. Eng. J.* 359 (2019) 186–196.
- [16] H. Yi, M. Yan, D. Huang, G. Zeng, C. Lai, M. Li, X. Huo, L. Qin, S. Liu, X. Liu, B. Li, H. Wang, M. Shen, Y. Fu, X. Guo, Synergistic effect of artificial enzyme and 2D nano-structured Bi₂WO₆ for eco-friendly and efficient biomimetic photocatalysis, *Appl. Catal. B: Environ.* 250 (2019) 52–62.
- [17] H. Lim, J. Lee, S. Jin, J. Kim, J. Yoon, T. Hyeon, Highly active heterogeneous Fenton catalyst using iron oxide nanoparticles immobilized in alumina coated mesoporous silica, *Chem. Commun. (Camb.)* (2006) 463–465.
- [18] W. Song, M. Cheng, J. Ma, W. Ma, C. Chen, J. Zhao, Decomposition of hydrogen peroxide driven by photochemical cycling of iron species in clay, *Environ. Sci. Technol.* 40 (2006) 4782–4787.
- [19] J.J. Zhu, P. Xiao, H.L. Li, S.A.C. Carabineiro, Graphitic carbon nitride: synthesis, properties, and applications in catalysis, *ACS Appl. Mater. Interfaces* 6 (2014) 16449–16465.
- [20] Y.T. Gong, M.M. Li, H.R. Li, Y. Wang, Graphitic carbon nitride polymers: promising catalysts or catalyst supports for heterogeneous oxidation and hydrogenation, *Green Chem.* 17 (2015) 715–736.
- [21] J. Liu, H.Q. Wang, M. Antonietti, Graphitic carbon nitride "reloaded": emerging applications beyond (photo) catalysis, *Chem. Soc. Rev.* 45 (2016) 2308–2326.
- [22] J. Jian, G. Jiang, R. van de Krol, B. Wei, H. Wang, Recent advances in rational engineering of multinary semiconductors for photoelectrochemical hydrogen generation, *Nano Energy* 51 (2018) 457–480.
- [23] P. Guo, Q. Ye, X. Yang, J. Zhang, F. Xu, D. Shchukin, B. Wei, H. Wang, Surface & grain boundary co-passivation by fluorocarbon based bifunctional molecules for perovskite solar cells with efficiency over 21%, *J. Mater. Chem. A Mater. Energy Sustain.* 7 (2019) 2497–2506.
- [24] Z.W. Zhao, Y.J. Sun, F. Dong, Graphitic carbon nitride based nanocomposites: a review, *Nanoscale* 7 (2015) 15–37.
- [25] S.C. Yan, Z.S. Li, Z.G. Zou, Photodegradation performance of g-C₃N₄ fabricated by directly heating melamine, *Langmuir* 25 (2009) 10397–10401.
- [26] A. Thomas, A. Fischer, F. Goettmann, M. Antonietti, J.-O. Mueller, R. Schloegl, J.M. Carlsson, Graphitic carbon nitride materials: variation of structure and morphology and their use as metal-free catalysts, *J. Mater. Chem.* 18 (2008) 4893–4908.
- [27] X. Wang, K. Maeda, A. Thomas, K. Takanabe, G. Xin, J.M. Carlsson, K. Domen, M. Antonietti, A metal-free polymeric photocatalyst for hydrogen production from water under visible light, *Nat. Mater.* 8 (2009) 76–80.
- [28] L. Shi, L. Liang, F. Wang, M. Liu, K. Chen, K. Sun, N. Zhang, J. Sun, Higher yield urea-derived polymeric graphitic carbon nitride with mesoporous structure and superior visible-light-responsive activity, *ACS. Sus. Chem. Eng.* 3 (2015) 3412–3419.
- [29] G. Zhang, J. Zhang, M. Zhang, X. Wang, Polycondensation of thiourea into carbon nitride semiconductors as visible light photocatalysts, *J. Mater. Chem.* 22 (2012) 8083–8091.
- [30] J.F. Perez-Benito, Reaction pathways in the decomposition of hydrogen peroxide catalyzed by copper(II), *J. Inorg. Bio. chem.* 98 (2004) 430–438.
- [31] D.-F. Weng, B.-W. Wang, Z.-M. Wang, S. Gao, Polymorphism of (H₂mela)₂[CuCl₅]Cl (mela = melamine): structures, transformation and magnetic properties, *CrystEngComm.* 13 (2011) 4683.
- [32] W.J. Ong, L.L. Tan, Y.H. Ng, S.T. Yong, S.P. Chai, Graphitic carbon nitride (g-C₃N₄)-based photocatalysts for artificial photosynthesis and environmental remediation: Are we a step closer to achieving sustainability? *Chem. Rev.* 116 (2016) 7159–7329.
- [33] Y. Wang, X.C. Wang, M. Antonietti, Polymeric graphitic carbon nitride as a heterogeneous organocatalyst from photochemistry to multipurpose catalysis to sustainable chemistry, *Angew. Chem. Int. Ed.* 51 (2012) 68–89.
- [34] C.Y. Zhou, C. Lai, D.L. Huang, G.M. Zeng, C. Zhang, M. Cheng, L. Hu, J. Wan, W.P. Xiong, M. Wen, X.F. Wen, L. Qin, Highly porous carbon nitride by supramolecular preassembly of monomers for photocatalytic removal of sulfamethazine under visible light driven, *Appl. Catal. B: Environ.* 220 (2018) 202–210.
- [35] C.H. Choi, L. Lin, S. Gim, S. Lee, H. Kim, X. Wang, W. Choi, Polymeric carbon nitride with localized aluminum coordination sites as a durable and efficient photocatalyst for visible light utilization, *ACS Catal.* 8 (2018) 4241–4256.
- [36] Y.B. Wang, X. Zhao, D. Cao, Y. Wang, Y.F. Zhu, Peroxymonosulfate enhanced visible light photocatalytic degradation bisphenol A by single-atom dispersed Ag mesoporous g-C₃N₄ hybrid, *Appl. Catal. B: Environ.* 211 (2017) 79–88.
- [37] D.L. Jiang, T.Y. Wang, Q. Xu, D. Li, S.C. Meng, M. Chen, Perovskite oxide ultrathin nanosheets/g-C₃N₄ 2D-2D heterojunction photocatalysts with significantly enhanced photocatalytic activity towards the photodegradation of tetracycline, *Appl. Catal. B: Environ.* 201 (2017) 617–628.
- [38] S.Z. Hu, X.Y. Qu, J. Bai, P. Li, Q. Li, F. Wang, L.J. Song, Effect of Cu(I)-N Active sites on the N₂ photofixation ability over flowerlike copper-doped g-C₃N₄ prepared via a novel molten salt-assisted microwave process: The experimental and density functional theory simulation analysis, *ACS. Sus. Chem. Eng.* 5 (2017) 6863–6872.
- [39] X. Wang, X. Chen, A. Thomas, X. Fu, M. Antonietti, Metal-containing carbon nitride compounds: a new functional organic-metal hybrid material, *Adv. Mater.* 21 (2009) 1609–1612.
- [40] Y. Li, J. Zhang, Q. Wang, Y. Jin, D. Huang, Q. Cui, G. Zou, Nitrogen-rich carbon nitride hollow vessels: synthesis, characterization, and their properties, *J. Phys. Chem. B* 114 (2010) 9429–9434.
- [41] T.F. Xu, D.N. Wang, L.L. Dong, H.B. Shen, W.Y. Lu, W.X. Chen, Graphitic carbon nitride co-modified by zinc phthalocyanine and graphene quantum dots for the efficient photocatalytic degradation of refractory contaminants, *Appl. Catal. B: Environ.* 244 (2019) 96–106.
- [42] B. Jurgens, E. Irran, J. Senker, P. Kroll, H. Muller, W. Schnick, Melem (2,5,8-triamino-tri-s-triazine), an important intermediate during condensation of melamine rings to graphitic carbon nitride: Synthesis, structure determination by X-ray powder diffractometry, solid-state NMR, and theoretical studies, *J. Am. Chem. Soc.* 125 (2003) 10288–10300.
- [43] S.-W. Bian, Z. Ma, W.-G. Song, Preparation and characterization of carbon nitride nanotubes and their applications as catalyst supporter, *J. Phys. Chem. C* 113 (2009) 8668–8672.
- [44] K. Gibson, J. Glaser, E. Milke, M. Marzini, S. Tragl, M. Binnewies, H.A. Mayer, H.J. Meyer, Preparation of carbon nitride materials by polycondensation of the single-source precursor aminodichlorotriazine (ADCT), *Mater. Chem. Phys.* 112 (2008) 52–56.
- [45] J. Gao, Y. Wang, S. Zhou, W. Lin, Y. Kong, A Facile One-step synthesis of Fe-Doped g-C₃N₄ nanosheets and their improved visible-light photocatalytic performance, *ChemCatChem.* 9 (2017) 1708–1715.
- [46] X.F. Li, J. Zhang, L.H. Shen, Y.M. Ma, W.W. Lei, Q.L. Cui, G.T. Zou, Preparation and characterization of graphitic carbon nitride through pyrolysis of melamine, *Appl. Phys. A-Mater. Sci. Process.* 94 (2009) 387–392.
- [47] V.N. Khabashesku, J.L. Zimmerman, J.L. Margrave, Powder synthesis and characterization of amorphous carbon nitride, *Chem. Mat.* 12 (2000) 3264–3270.
- [48] S. Cao, J. Low, J. Yu, M. Jaroniec, Polymeric photocatalysts based on graphitic

carbon nitride, *Adv. Mater.* 27 (2015) 2150–2176.

[50] S.B. Yang, Y.J. Gong, J.S. Zhang, L. Zhan, L.L. Ma, Z.Y. Fang, R. Vajtai, X.C. Wang, P.M. Ajayan, Exfoliated graphitic carbon nitride nanosheets as efficient catalysts for hydrogen evolution under visible light, *Adv. Mater.* 25 (2013) 2452–2456.

[51] L.Q. Yang, J.F. Huang, L. Shi, L.Y. Cao, Q. Yu, Y.N. Jie, J. Fei, H.B. Ouyang, J.H. Ye, A surface modification resultant thermally oxidized porous g-C₃N₄ with enhanced photocatalytic hydrogen production, *Appl. Catal. B: Environ.* 204 (2017) 335–345.

[52] N. Jiang, L. Lyu, G. Yu, L. Zhang, C. Hu, A dual-reaction-center Fenton-like process on C≡N–Cu linkage between copper oxides and defect-containing g-C₃N₄ for efficient removal of organic pollutants, *J. Mater. Chem. A Mater. Energy Sustain.* 6 (2018) 17819–17828.

[53] R.V. Jagadeesh, A.-E. Surkus, H. Junge, M.-M. Pohl, J. Radnik, J. Rabeh, H. Huan, V. Schuermann, A. Brueckner, M. Beller, Nanoscale Fe₂O₃-Based catalysts for selective hydrogenation of nitroarenes to anilines, *Science* 342 (2013) 1073–1076.

[54] A. Savini, A. Bucci, M. Nocchetti, R. Vivani, H. Idriss, A. Macchioni, Activity and recyclability of an iridium-EDTA water oxidation catalyst immobilized onto rutile TiO₂, *ACS Catal.* 5 (2015) 264–271.

[55] G.X. Chen, C.F. Xu, X.Q. Huang, J.Y. Ye, L. Gu, G. Li, Z.C. Tang, B.H. Wu, H.Y. Yang, Z.P. Zhao, Z.Y. Zhou, G. Fu, N.F. Zheng, Interfacial electronic effects control the reaction selectivity of platinum catalysts, *Nat. Mater.* 15 (2016) 564–569.

[56] D. Manoj, R. Saravanan, J. Santhanakrishni, S. Agarwal, V.K. Gupta, R. Boukherroub, Towards green synthesis of monodisperse Cu nanoparticles: an efficient and high sensitive electrochemical nitrite sensor, *Sens. Actuators B Chem.* 266 (2018) 873–882.

[57] S. Xu, H. Zhu, W. Cao, Z. Wen, J. Wang, C.P. Francois-Xavier, T. Wintgens, Cu-Al₂O₃-g-C₃N₄ and Cu-Al₂O₃-C-dots with dual-reaction centres for simultaneous enhancement of Fenton-like catalytic activity and selective H₂O₂ conversion to hydroxyl radicals, *Appl. Catal. B: Environ.* 234 (2018) 223–233.

[58] Y.-D. Zhu, J. Peng, L.-P. Jiang, J.-J. Zhu, Fluorescent immunosensor based on Cu nanoparticles for sensitive detection of cancer biomarker, *Analyst* 139 (2014) 649–655.

[59] C. Yang, C. Zhang, L. Liu, Excellent degradation performance of 3D hierarchical nanoporous structures of copper towards organic pollutants, *J. Mater. Chem. A Mater. Energy Sustain.* 6 (2018) 20992–21002.

[60] Z. Li, C. Kong, G.X. Lu, Visible photocatalytic water splitting and photocatalytic two-electron oxygen formation over Cu- and Fe-Doped g-C₃N₄, *J. Phys. Chem. C.* 120 (2016) 56–63.

[61] H.A. Bicalho, J.L. Lopez, I. Binatti, P.F.R. Batista, J.D. Ardisson, R.R. Resende, E. Lorencon, Facile synthesis of highly dispersed Fe(II)-doped g-C₃N₄ and its application in Fenton-like catalysis, *Mol. Catal.* 435 (2017) 156–165.

[62] J. Ma, Q. Yang, Y. Wen, W. Liu, Fe-g-C₃N₄/graphitized mesoporous carbon composite as an effective Fenton-like catalyst in a wide pH range, *Appl. Catal. B: Environ.* 201 (2017) 232–240.

[63] R. Huang, Y. Liu, Z. Chen, D. Pan, Z. Li, M. Wu, C.-H. Shek, C.M.L. Wu, J.K.L. Lai, Fe-species-loaded mesoporous MnO₂ superstructural requirements for enhanced catalysis, *ACS Appl. Mater. Interfaces* 7 (2015) 3949–3959.

[64] Y.Y. Sheng, Y. Sun, J. Xu, J. Zhang, Y.F. Han, Fenton-like degradation of rhodamine B over highly durable Cu-embedded alumina: kinetics and mechanism, *AIChE J.* 64 (2018) 538–549.

[65] J. Gao, J. Wang, X. Qian, Y. Dong, H. Xu, R. Song, C. Yan, H. Zhu, Q. Zhong, G. Qian, J. Yao, One-pot synthesis of copper-doped graphitic carbon nitride nanosheet by heating Cu–melamine supramolecular network and its enhanced visible-light-driven photocatalysis, *J. Solid State Chem.* 228 (2015) 60–64.

[66] L. Wang, D.B.A. Yan, L. Lyu, C. Hu, N. Jiang, L.L. Zhang, Notable light-free catalytic activity for pollutant destruction over flower-like BiOI microspheres by a dual-reaction-center Fenton-like process, *J. Colloid Interface Sci.* 527 (2018) 251–259.

[67] L. Lyu, L.L. Zhang, Q.Y. Wang, Y.L. Nie, C. Hu, Enhanced Fenton catalytic efficiency of gamma-Cu-Al₂O₃ by sigma-Cu²⁺-Ligand complexes with aromatic pollutant degradation, *Environ. Sci. Technol.* 49 (2015) 8639–8647.

[68] Z. Matuszak, K.J. Reszka, C.F. Chignell, Reaction of melatonin and related indoles with hydroxyl radicals: EPR and spin trapping investigations, *Free Radical Biol. Med.* 23 (1997) 367–372.